aqueous tubes cladded with the nanoparticle surfactants were smaller in diameter and exceptionally long, reminiscent of glass wool (Fig. 3G) except that the structures are fully liquid. The 3D nature of the morphology, the continuity of the tubular structures, and the cladding of the interfaces by the nanoparticle surfactant are evident. Thus, simply by stirring, a bicontinuous jammed system—a "bijel" type of morphology—is achieved without the need to modify and tune the surface chemistry of the nanoparticle to achieve neutral wetting, which is necessary to confine the nanoparticles to the liquid/liquid interface and impart long-term stability to the morphology (*13*, *14*). The carboxylate-amine interactions between the nanoparticles and functionalized silicone oil are self-regulating, maximizing the reduction in the interfacial energy, overcoming thermal energies and stabilizing the nanoparticle surfactants at the interface.

When the monofunctional end-capped silicone oil was replaced with a difunctional PDMS, capped on both ends with primary amines, the nanoparticle surfactant assemblies were stabilized even further, as the PDMS chains bridge adjacent nanoparticles, effectively cross-linking the jammed nanoparticle assembly (Fig. 4A). Shown in Fig. 4, B to E, are two drops of water with polystyrene nanoparticles that were suspended in silicone oil containing the difunctional PDMS. The length of time that the drop at the bottom was in contact with the silicone oil is 2 min, whereas the contact time of the upper drop is 30 s. A 4.6-kV/cm electric field is applied, and the drop at the bottom does not deform, whereas the drop at the top deforms. Even though the interfacial energy of the drop at the bottom is lower, due to the increase in the number of nanoparticle surfactants formed at the interface, the cross-linking of the nanoparticle surfactants is greater, preventing the deformation of the drop (movies S6 and S7). The very strong resistance of the drop to deformation demonstrates an alternate route by which drops of different shapes can be stabilized.

We have demonstrated a simple route to produce and stabilize fluid drops having shapes far removed from their equilibrium spherical shape, using the in situ formation of nanoparticle surfactants. The increased interfacial activity of the nanoparticle surfactants stabilized the assemblies against desorption, allowing them to jam at the interface, arresting change in the drop shape, and imparting long-term stability to drops with unusual shapes. The sequential application of external fields in different directions leads to local unjamming and jamming of the assemblies, enabling the shape of the drop to be tailored into a wide range of unusual shapes. We are currently investigating the possibility of stabilizing asymmetric shapes to determine the importance on the jamming process. Both electric and shear fields were used to deform the drops, although other fields, like magnetic and ultrasonic fields, are also being investigated. Cross-linking the nanoparticle surfactant assemblies at the interface is shown to increase the stability of the drop shape. These stabilized assemblies provide easy routes for encapsulation, bicontinuous flow (microfluidic devices) or separations media, delivery vehicles, and reaction platforms.

References and Notes

1. R. Hong *et al.*, *J. Am. Chem. Soc.* **128**, 1078–1079 (2006).
2. Y. Q. Shi, F. Li, Y. W. Chen, *New J. Chem.* **37**, 236–244 (2013).
3. K. Bramhaiah, N. S. John, *RSC Adv.* **3**, 7765 (2013).
4. D. Lee, D. A. Weitz, *Adv. Mater.* **20**, 3498–3503 (2008).
5. C. N. R. Rao, K. P. Kalyanikutty, *Acc. Chem. Res.* **41**, 489–499 (2008).
6. A. D. Dinsmore *et al.*, *Science* **298**, 1006–1009 (2002).
7. Y. Lin, H. Skaff, T. Emrick, A. D. Dinsmore, T. P. Russell, *Science* **299**, 226–229 (2003).
8. A. B. Subramaniam, M. Abkarian, L. Mahadevan, H. A. Stone, *Nature* **438**, 930 (2005).
9. M. Abkarian *et al.*, *Phys. Rev. Lett.* **99**, 188301 (2007).
10. A. B. Pawar, M. Caggioni, R. Ergun, R. W. Hartel, P. T. Spicer, *Soft Matter* **7**, 7710 (2011).
11. K. Stratford, R. Adhikari, I. Pagonabarraga, J. C. Desplat, M. E. Cates, *Science* **309**, 2198–2201 (2005).
12. E. M. Herzig, K. A. White, A. B. Schofield, W. C. K. Poon, P. S. Clegg, *Nat. Mater.* **6**, 966–971 (2007).
13. B. P. Binks, S. O. Lumsdon, *Langmuir* **16**, 8622–8631 (2000).
14. B. P. Binks, T. S. Horozov, *Colloidal Particles at Liquid Interfaces* (Cambridge Univ. Press, Cambridge, 2006).
15. L. Li *et al.*, *Nano Lett.* **11**, 1997–2003 (2011).
16. C. Zeng, F. Brau, B. Davidovitch, A. D. Dinsmore, *Soft Matter* **8**, 8582 (2012).
17. P. S. Clegg *et al.*, *J. Phys. Condens. Matter* **17**, S3433 (2005).
18. P. S. Clegg *et al.*, *Langmuir* **23**, 5984–5994 (2007).
19. H. L. Cheng, S. S. Velankar, *Langmuir* **25**, 4412–4420 (2009).
20. J. W. Tavacoli, J. H. J. Thijssen, A. B. Schofield, P. S. Clegg, *Adv. Funct. Mater.* **21**, 2020–2027 (2011).
21. S. A. F. Bon, S. D. Mookhoek, P. J. Colver, H. R. Fischer, S. van der Zwaag, *Eur. Polym. J.* **43**, 4839–4842 (2007).
22. D. Orsi, L. Cristofolini, G. Baldi, A. Madsen, *Phys. Rev. Lett.* **108**, 105701 (2012).
23. Y. Lin *et al.*, *Langmuir* **21**, 191–194 (2005).
24. A. J. Liu, S. R. Nagel, *Nature* **396**, 21–22 (1998).
25. G. Taylor, *Proc. R. Soc. London A Math. Phys. Sci.* **280**, 383–397 (1964).
26. O. Vizika, D. A. Saville, *J. Fluid Mech.* **239**, 1 (1992).
27. D. A. Saville, *Annu. Rev. Fluid Mech.* **29**, 27–64 (1997).
28. H. A. Stone, J. R. Lister, M. P. Brenner, *Proc. R. Soc. London A* **455**, 329–347 (1999).
29. J. W. Ha, S. M. Yang, *J. Fluid Mech.* **405**, 131–156 (2000).
30. J. Q. Feng, T. C. Scott, *J. Fluid Mech.* **311**, 289 (1996).

Acknowledgments: This work was supported by the U.S. Department of Energy Office of Basic Energy Science through contract DE-FG02-04ER46126. There are no conflicts of interest.

Supplementary Materials

www.sciencemag.org/content/342/6157/460/suppl/DC1
Materials and Methods
Figs. S1 to S4
Movies S1 to S7

8 July 2013; accepted 25 September 2013
10.1126/science.1242852

Mass-Independent Oxygen Isotopic Partitioning During Gas-Phase SiO_2 Formation

Subrata Chakraborty,* Petia Yanchulova, Mark H. Thiemens

Meteorites contain a wide range of oxygen isotopic compositions that are interpreted as heterogeneity in solar nebula. The anomalous oxygen isotopic compositions of refractory mineral phases may reflect a chemical fractionation process in the nebula, but there are no experiments to demonstrate this isotope effect during particle formation through gas-phase reactions. We report experimental results of gas-to-particle conversion during oxidation of silicon monoxide that define a mass-independent line (slope one) in oxygen three-isotope space of $^{18}O/^{16}O$ versus $^{17}O/^{16}O$. This mass-independent chemical reaction is a potentially initiating step in nebular meteorite formation, which would be capable of producing silicate reservoirs with anomalous oxygen isotopic compositions.

The oxygen isotopic composition of high-temperature mineral phases in the first condensates in the protoplanetary disk, calcium-aluminum-rich inclusions (CAIs), are distributed along a slope one line in an oxygen three-isotope plot ($^{18}O/^{16}O$ versus $^{17}O/^{16}O$) with a large and equal depletion in ^{17}O and ^{18}O [~50 per mil (‰) with respect to the terrestrial composition] (*1*). Most chondrules (glassy globular condensates) formed shortly (<1 million years) after CAIs (*2*) display an oxygen isotopic distribution along an approximate slope 1 line, with about equal ^{17}O and ^{18}O enrichments over CAIs (*3*, *4*). The oxygen isotopic distributions are notable because of their departure from the normal terrestrial mass-dependent (MD) fractionation line observed for equilibrium and kinetic fractionation processes of slope one-half (*5*, *6*). Defining the source of the anomalous isotopic distribution of oxygen is critical in the elucidation of the overall formation and evolutionary events in the early solar system.

After the failure to find meteoritic supernova debris signatures, the initially proposed nuclear

Department of Chemistry and Biochemistry, University of California, San Diego, La Jolla, CA 92093–0356, USA.
*Corresponding author. E-mail: subrata@ucsd.edu

theory (*1*) was largely abandoned, and chemical, particularly photochemical, theories took precedence as the favored explanation for the observed oxygen isotopic distribution. Photochemical isotopic self-shielding of CO (*7*) has been proposed on the basis of the predissociative nature (isotopologue-specific absorption lines) in the vacuum ultraviolet spectral region of CO, a common phenomenon in molecular clouds (*8*). Ozone formation was the first demonstration of a mass-independent (MI) fractionation process in a chemical reaction (*9*). Since this discovery, the potential for producing a CAI-like isotopic compositional trend in a gas-phase symmetry-driven recombination reaction has been suggested (*9*–*11*). Marcus (*12*) introduced a symmetry-based grain-surface assisted theoretical treatment of recombination of adsorbed species, e.g., O and SiO, to explain the compositions of CAIs. At present, there are no experiments that determine the isotopic fractionation induced by the conversion of gas-phase nebular oxygen species to solid species, which is a key step in the early evolutionary stage of the solar system.

Here, we present results of the measurement of oxygen isotopic compositions of SiO_2 solids generated via gas-phase reactions under controlled experimental conditions. In these experiments, ultrahigh purity (UHP) SiO nuggets were lased with an excimer laser [Lambda Physik Compex 110 (Coherent Incorporated, Santa Clara, California), KrF, 248 nm] inside a vacuum chamber at two different initial conditions: set I, in the presence of UHP O_2, and set II, in mixtures of UHP O_2 and H_2 of differing proportions. Lasing of SiO generates a plume of neutral SiO gas (see supplementary materials), which reacts with the gases inside the chamber to form silicon dioxide particles throughout the chamber. In set III experiments, the product SiO_2 is formed via both mechanisms of set I and set II (as subsets) experiments, and the products were collected for analysis. Scanning electron microscopic analysis provided the stoichiometry of SiO_2 for the product solids for all cases (fig. S2).

The measured oxygen isotopic compositions of SiO_2 formed in set I–type experiments (without H_2) show MD fractionation, whereas those produced in set II–type experiments (with H_2) reflect MI fractionation (Fig. 1 and table S1). The corresponding isotopic compositions of the residual oxygen reservoirs are fractionated in MD and MI fashion, respectively, for set I and set II experiments (fig. S3 and tables S2 and S3). The extent of the MI component in SiO_2, measured by $\Delta^{17}O$ ($=\delta^{17}O - 0.516 \times \delta^{18}O$), increases with increasing initial H_2/O_2 ratio, and the maximum $\Delta^{17}O$ value was ~1.7‰, measured at an H_2/O_2 ratio of 25.6. The higher ambient gas pressure suppresses the expansion of the laser plume and also rapidly cools the plume by collisional deactivation limiting the extent of oxidation in the higher ratio and pressure experiments (see supplementary text).

Comparing the expected oxidation reactions 1 to 4 and 1 to 10 for set I and set II experiments (Table 1), respectively, and their corresponding experimental results (Fig. 1, fig. S3, and tables S1 to S3), we suggest that the observed MI composition in the residual oxygen and product SiO_2 may not be due to ozone formation [known to generate a MI composition (*9*)]. Set I–type experiments are the most oxidative and kinetically favor ozone formation compared with set II types. The results from set I experiments are strictly MD (Fig. 1 and fig. S3) and cannot involve ozone formation. Analyzing the entire data set, we observed a MI composition only when H_2 is

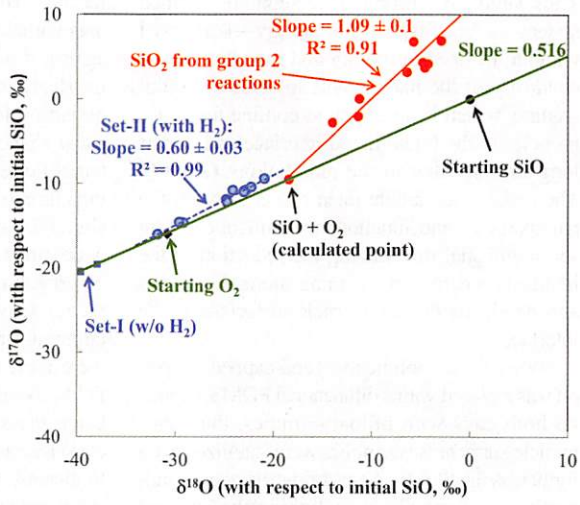

Fig. 1. Measured oxygen isotopic compositions in three-isotope plot. The compositions of product SiO_2 from set I– and set II–types experiments in set III are shown in blue squares and circles, respectively, with respect to the initial SiO composition. Compositions of the starting SiO and oxygen and product SiO_2 from set I–type experiments all lie on a line with a MD slope of 0.516. The SiO_2 formed in set II–type experiments show MI compositions with a slope value of 0.6. The calculated isotopic compositions of SiO_2 formed by group 2 reactions (OH dominated, see supplementary text) lie on a regression line with a slope value of 1.09 ± 0.1. The standard deviation of data presented here are ± 0.2‰ (much smaller than the size of the symbols).

Table 1. List of relevant reactions. Relevant reactions for set I and set II experiments.

Set I–type experiments	Set II–type experiments	Reaction number
	Group 1	
$SiO + O_2 \rightarrow SiO_2 + O$	$SiO + O_2 \rightarrow SiO_2 + O$	1
$SiO + O \rightarrow SiO_2$	$SiO + O \rightarrow SiO_2$	2
$O_2 + h\nu \rightarrow O + O$	$O_2 + h\nu \rightarrow O + O$	3
$O + O_2 + M \rightarrow O_3 + M$	$O + O_2 + M \rightarrow O_3 + M$	4
	Group 2	
	$O + H_2 + M \rightarrow OH + H + M$	5
	$OH + H_2 \rightarrow H_2O + H$	6
	$SiO + OH \rightarrow SiO_2 + H$	7
	$SiO + H_2O \rightarrow SiO_2 + OH$	8
	$H + O_2 + M \rightarrow HO_2 + M$	9
	$SiO + HO_2 \rightarrow SiO_2 + OH$	10

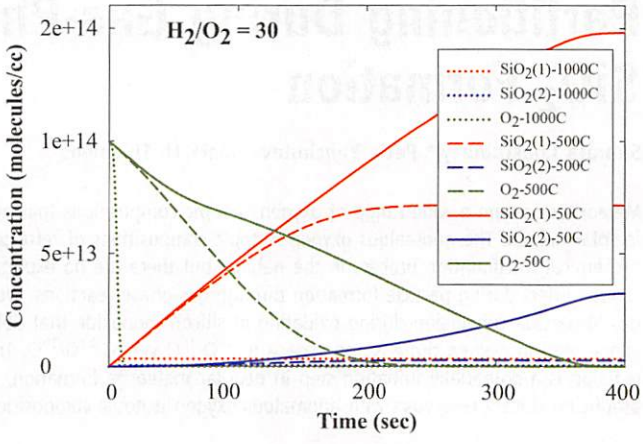

Fig. 2. Results of kinetic model simulation. Time-dependent change in concentrations of SiO_2 formed via group 1 and group 2 reactions and the concentration of O_2 for the simulation run with H_2/O_2 ratio of 30 is shown for three different temperatures. The SiO_2 amount measured in the experiments best matched the simulation run of effective chamber temperature of 50°C. Although the temperature of the laser plume is high (>1000°C), the estimated volume of the laser plume is only ~1/100 of the chamber volume, and, therefore, the match at lower temperature (50°C) with the experiment is reasonable. The result shows that, in set II–type experiments, group 1 reactions are the dominant source of SiO_2 formation, whereas group 2 reactions contribute only 11 to 18% of the total SiO_2.

present, requiring reactions 7, 8, and 10 to be the source of the MI composition.

Because reaction 9 is a MI process (*13*), there is a possibility that the isotopic composition measured in these experiments was acquired during oxidation by HO_2, a product of reaction 9, which possesses a MI composition. To test HO_2 reaction channels, we performed photolysis of a mixture of O_2 and H_2 in a glass chamber (without SiO) with ultraviolet photons from the same laser as a control. The residual oxygen was collected (after separating it from H_2 and water), and the oxygen isotopic composition was determined to be MD (fig. S3), indicating that the MI character measured in the set II experiments does not originate from HO_2 species via reaction channel 9.

The oxidation of CO by OH produces CO_2 of MI composition (*14*, *15*); thus reaction 7 (SiO + OH = SiO_2 + H) may be the source of the measured MI effect because both CO and SiO possess a homologous valence electron configuration in their ground states (*16*). On the basis of symmetry considerations, it has been proposed that a gas-phase MI effect may arise from the reaction O + SiO → SiO_2 (*17*). An analogous reaction, O + CO → CO_2, has experimentally demonstrated notable mass-independently fractionated products (*18*, *19*). However, the results from set I experiments do not reflect the fractionation effects of this process. In set I experiments, SiO_2 formed through reactions 1 and 2 may have a potential for isotope exchange between O_2 and O, and the original isotopic signature (MI) from reaction 2 (e.g., O + SiO → SiO_2) may be removed by exchange, as well as by the MD SiO_2 produced by reaction 1 (e.g., O_2 + SiO → SiO_2 + O).

A vibrationally excited transition state (COOH*) has been predicted for the CO + OH → CO_2 + H reaction (*20*–*22*), and the existence of a vibrationally excited intermediate was demonstrated (*23*). A similar intermediate state (SiOOH)* for the OH + SiO → SiO_2 + H reaction is feasible, and it is via this excited state that the observed MI effect would be generated. The relevant source would be the deactivation of intermediate states leading to isotope selectivity in the product phase, as is the case for ozone. There is no overall agreement on the mechanism for ozone formation, although symmetry is generally considered to be the ultimate source (*24*).

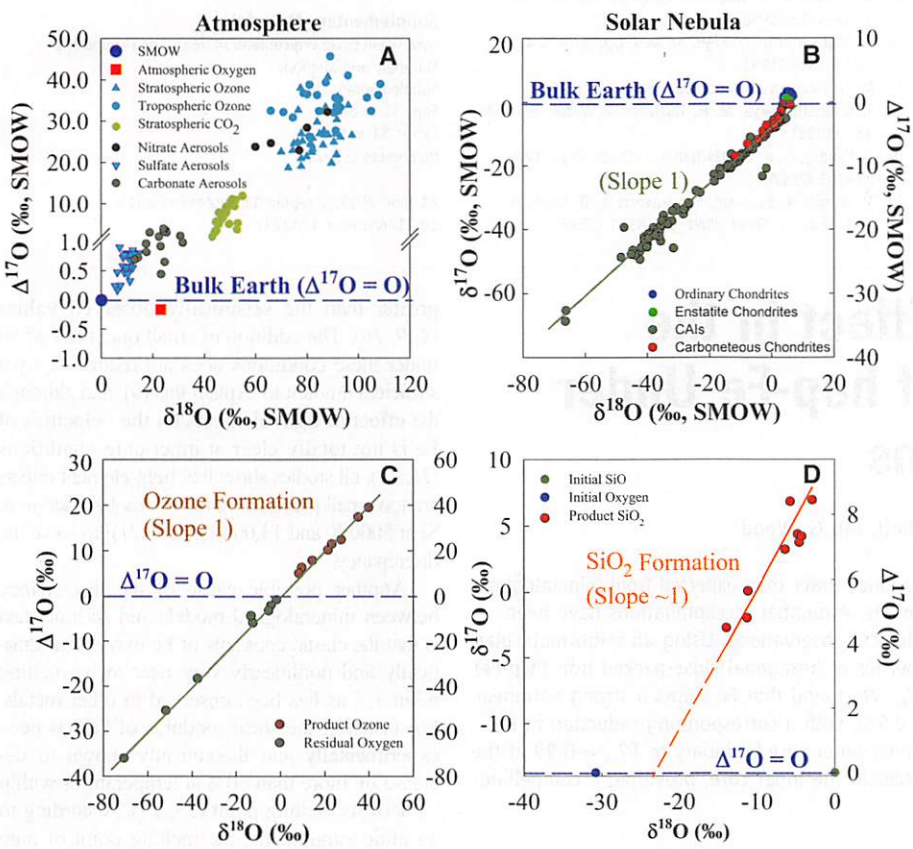

Fig. 3. Similarity of oxygen isotopic distribution in atmosphere and meteorites. Left and right panels represent Earth's atmosphere and meteorites, respectively. **(A)** The existence of positive and negative $\Delta^{17}O$ reservoirs in the atmosphere. **(B)** The presence of positive and negative $\Delta^{17}O$ reservoirs in the solar nebula (over a slope of ~1 line). **(C)** The composition of product ozone and residual oxygen for the ozone formation experiment in the laboratory. **(D)** The compositions of SiO_2 formed in the present experiments. The δ values are normalized with starting oxygen and SiO compositions, respectively, for (C) and (D). See supplementary materials for a full list of references used for this compilation.

SiO_2 samples collected in set II–type experiments are formed via multiple reaction channels (Table 1). We developed a chemical kinetic network model including 17 different species and 30 different reactions relevant to the experiments. Time-dependent concentration variations of different species were recorded in this model by setting up appropriate differential equations (see supplementary text). The simulation solutions depict that a significant proportion of SiO_2 (82 to 89%) is produced via oxidation in group 1 reactions (by O_2 and O; MD in nature) with the remaining channel produced by group 2 oxidation reactions (Fig. 2 and table S4). The model production of SiO_2 via H_2O_2 oxidation is negligible and consequently not specifically listed in Table 1. Because the contributions from group 2 reactions in the total production of SiO_2 are much smaller (<18%), the measured MI composition in set II–type experiments are diluted by MD contributions from group 1 reactions (Fig. 1).

By considering the fractionations for the group 1 reactions to be those measured in set I reactions and the above-mentioned fractions (of product from groups 1 and 2), we performed an isotopic mass-balance calculation to determine the compositions of SiO_2 formed via group 2 reactions (see supplementary text), which define a line of slope = 1.09 ± 0.1 (1-σ SD) passing through the calculated SiO_2 composition ($\delta^{18}O = -18.4‰$, $\delta^{17}O = -9.5‰$) formed by the measured SiO + O_2 reaction (Fig. 1 and supplementary text). The scatter in the calculated data set may be due to the use of a simplified treatment by grouping the reactions in two, where there are six different reactions in group 2, and, based on kinetics, they have different yields at different subsets of experiments because of variation in pressures (table S3). The kinetic simulation shows that among all group 2 reactions (which contribute <18% of total SiO_2 production) more than 90% of SiO_2 forms via OH oxidation. It may be surmised from the observations that the SiO + OH reaction follows a slope close to unity.

SiO is a relevant solar nebular species detected in young protoplanetary nebulae and other astronomical objects (*25*, *26*) and is oxidized by OH in the early nebula (*27*–*29*). It is plausible that, in the hot (>1000 K) inner solar nebula, SiO oxidation through OH is an initiating reaction in solid silicate formation. Our results demonstrate that the MI composition of meteoritic silicates could be initially generated via OH oxidation of the more reduced SiO, which proceeds along a slope one line. However, transiting through an intermediate excited state is not equilibrium in nature, and the traditional isotopic fractionation calculated on the basis of reduced partition functions (*5*) diminishes at high temperature limits and is not applicable.

Earth's atmosphere may be isotopically relevant in comparison to the solar nebula because both systems have oxygen reservoirs consisting of relative positive and negative MI anomalies (Fig. 3, A and B). The oxygen-bearing species

acquire MI signatures from the ozone formation reaction (*9*) (Fig. 3C) via atomic oxygen interaction, creating small reservoirs with large positive $\Delta^{17}O$ and vice versa (e.g., atmospheric O_2 with negative $\Delta^{17}O$). Similarly, in meteorites, a large negative MI effect in minor phases (CAIs, chondrules and matrices in carbonaceous chondrites, and Ureilites) and a smaller positive MI effect in the more abundant classes (by mass, for example, ordinary chondrites and Rumaruti classes) are observed. Meteoritic negative and positive $\Delta^{17}O$ reservoirs could have been originated during the actual gas-to-particle formation process as experimentally demonstrated here (Fig. 3D). Solar system oxygen is more complicated, and the initial solar nebular bulk composition is inadequately defined. The measured oxygen composition of solar wind from Genesis concentrator is enriched in ^{16}O compared with CAIs (*30*); but the oxygen isotopic fractionation between the solar photosphere and the solar wind is not well established and presently an open question.

The final step in the formation of solid silicate from the gas-dominated nebula is a chemical reaction, and the fractionation occurring in this process should be considered regardless of which model is invoked. This reaction, if it occurs in a solar nebula at high temperature, the effect may be larger than observed in the present experiments given the inverse temperature dependency as observed for ozone (*31*). Last, the observed MI effect is unique to oxygen. The terminal atom regulates the formation and stabilization of vibrationally excited symmetrically structured molecules (*31*, *32*), and oxygen plays this critical role in SiO_2. This accounts for why other isotope systems (e.g., Si) do not correlate with oxygen and produce an observable symmetry-dependent fractionation. Carbon and hydrogen are candidates but only possess two stable isotopes and cannot prove the effect, and sulfur, with multiple valence states and exchangeability, is not ideal for preserving the effect.

References and Notes

1. R. N. Clayton, L. Grossman, T. K. Mayeda, *Science* **182**, 485–488 (1973).
2. J. N. Connelly *et al.*, *Science* **338**, 651–655 (2012).
3. R. N. Clayton, *Annu. Rev. Earth Planet. Sci.* **35**, 1–19 (2007).
4. M. H. Thiemens, *Annu. Rev. Earth Planet. Sci.* **34**, 217–262 (2006).
5. H. C. Urey, *J. Chem. Soc.* **1947**, 562–581 (1947).
6. M. F. Miller, *Geochim. Cosmochim. Acta* **66**, 1881–1889 (2002).
7. J. R. Lyons, E. D. Young, *Nature* **435**, 317–320 (2005).
8. J. Bally, W. D. Langer, *Astrophys. J.* **255**, 6 (1982).
9. M. H. Thiemens, J. E. Heidenreich 3rd, *Science* **219**, 1073–1075 (1983).
10. J. E. Heidenreich, M. H. Thiemens, *J. Chem. Phys.* **84**, 2129 (1986).
11. Y. Q. Gao, R. A. Marcus, *Science* **293**, 259–263 (2001).
12. R. A. Marcus, *J. Chem. Phys.* **121**, 8201–8211 (2004).
13. J. Savarino, M. H. Thiemens, *J. Phys. Chem. A* **103**, 9221–9229 (1999).
14. T. Röckmann *et al.*, *Science* **281**, 544–546 (1998).
15. A. K. Huff, M. H. Thiemens, *Geophys. Res. Lett.* **25**, 3509–3512 (1998).
16. E. Bouisset *et al.*, *J. Phys. At. Mol. Opt. Phys.* **24**, 1609–1614 (1991).
17. M. H. Thiemens, *Science* **283**, 341–345 (1999).
18. S. K. Bhattacharya, M. H. Thiemens, *Z. Natur. Teil A* **44**, 435 (1989).
19. A. Pandey, S. K. Bhattacharya, *J. Chem. Phys.* **124**, 234301 (2006).
20. M. Alagia, N. Balucani, P. Casavecchia, D. Stranges, G. G. Volpi, *J. Chem. Phys.* **98**, 8341 (1993).
21. J. Li *et al.*, *J. Chem. Phys.* **136**, 041103 (2012).
22. X. Song, J. Li, H. Hou, B. Wang, *J. Chem. Phys.* **125**, 6 (2006).
23. M. Brouard, D. W. Hughes, K. S. Kalogerakis, J. P. Simons, *J. Phys. Chem. A* **102**, 9559–9564 (1998).
24. M. H. Thiemens, S. Chakraborty, G. Dominguez, *Annu. Rev. Phys. Chem.* **63**, 155–177 (2012).
25. S.-H. Cho, J. Kim, *Astron. J.* **144**, 129 (2012).
26. V. Bujarrabal, J. Alcolea, P. Planesas, *Astron. Astrophys.* **257**, 14 (1992).
27. G. J. MacPherson, A. Boss, *Proc. Natl. Acad. Sci. U.S.A.* **108**, 19152–19158 (2011).
28. F. J. Ciesla, J. N. Cuzzi, *Icarus* **181**, 178–204 (2006).
29. C. Walsh, T. J. Millar, H. Nomura, *Astrophys. J.* **722**, 1607 (2010).
30. K. D. McKeegan *et al.*, *Science* **332**, 1528–1532 (2011).
31. Y. Q. Gao, R. A. Marcus, *J. Chem. Phys.* **116**, 137 (2002).
32. M. V. Ivanov, D. Babikov, *Proc. Natl. Acad. Sci. U.S.A.*, published online 19 February 2013 (10.1073/pnas.1215464110).

Acknowledgments: The authors thank the three anonymous reviewers for their helpful critical comments, which helped improve the manuscript. S.C. and M.H.T. acknowledge funding support from NASA Cosmochemistry (NNX09AG93G) and Origins in Solar System (NNX11AB39G) programs. We acknowledge G. Dominguez for helping to develop the kinetic model and helpful discussion with members of the Thiemens research group. Data described in this paper are presented in supplementary materials.

Supplementary Materials

www.sciencemag.org/content/342/6157/463/suppl/DC1
Materials and Methods
Supplementary Text
Figs. S1 to S4
Tables S1 to S5
References (*33*–*70*)

21 June 2013; accepted 11 September 2013
10.1126/science.1242237

Strong Premelting Effect in the Elastic Properties of hcp-Fe Under Inner-Core Conditions

Benjamí Martorell,* Lidunka Vočadlo, John Brodholt, Ian G. Wood

The observed shear-wave velocity V_S in Earth's core is much lower than expected from mineralogical models derived from both calculations and experiments. A number of explanations have been proposed, but none sufficiently explain the seismological observations. Using ab initio molecular dynamics simulations, we obtained the elastic properties of hexagonal close-packed iron (hcp-Fe) at 360 gigapascals up to its melting temperature T_m. We found that Fe shows a strong nonlinear shear weakening just before melting (when $T/T_m > 0.96$), with a corresponding reduction in V_S. Because temperatures range from $T/T_m = 1$ at the inner-outer core boundary to $T/T_m \approx 0.99$ at the center, this strong nonlinear effect on V_S should occur in the inner core, providing a compelling explanation for the low V_S observed.

Earth's inner core is predominantly made of iron (Fe), but it is commonly assumed to contain 5 to 10% Ni (*1*) and also light elements such as Si, C, and S, ~2 to 3 weight percent in total (*1*, *2*). Seismic wave velocities through the inner core are known, but at present, seismological and mineralogical models for the inner core do not agree (*3*–*9*). A major discrepancy between the observed seismic data and current mineralogical models derived from ab initio calculations is that these mineralogical models predict a shear-wave velocity V_S that is up to 30% greater than the seismically observed values (*4*, *9*, *10*). The addition of small quantities of Ni under these conditions does not reduce V_S by a sufficient amount to explain this (*9*), and although the effect of light elements on the velocities of Fe is not totally clear at inner-core conditions (*11*, *12*), all studies show that light-element effects are too small [<5% in V_S for 7% molar fraction in Si at 5000 K and 13,000 kg m^{-3} (*11*)] to solve the discrepancy.

Another possible cause of the discrepancy between mineralogical models and seismic data is that the elastic constants of Fe may soften drastically and nonlinearly very near to its melting point T_m, as has been observed in other metals. For instance, the shear modulus of Sn has been experimentally and theoretically shown to decrease by more than 50% at temperatures within ~1% of its melting point (*13*, *14*). According to ab initio simulations, the melting point of pure Fe at the conditions of the inner core is in the range 6200 to 6900 K (*15*–*17*) according to phase coexistence calculations (solid and liquid), with upper limit estimates up to 7500 K (*18*) when only the solid phase is heated until melting. The highest temperature for which the elastic properties of hcp-Fe have been obtained computationally is 6000 K (*5*); however, relative to the melting

Department of Earth Sciences, University College London, London WC1E 6BT, UK.
*Corresponding author. E-mail: b.massip@ucl.ac.uk